How to cite: *Angew. Chem. Int. Ed.* **2024**, *63*, e202318539
doi.org/10.1002/anie.202318539

Controlled Release Hot Paper

Bioorthogonal "Click and Release" Reaction-Triggered Aggregation of Gold Nanoparticles Combined with Released Lonidamine for Enhanced Cancer Photothermal Therapy

Xiao Yan[+], Ke Li[+], Tian-Qiu Xie, Xiao-Kang Jin, Cheng Zhang, Qian-Ru Li, Jun Feng, Chuan-Jun Liu, and Xian-Zheng Zhang**

Abstract: Cancer has been the most deadly disease, and 13 million cancer casualties are estimated to occur each year by 2030. Gold nanoparticles (AuNPs)-based photothermal therapy (PTT) has attracted great interest due to its high spatiotemporal controllability and noninvasiveness. Due to the trade-off between particle size and photothermal efficiency of AuNPs, rational design is needed to realize aggregation of AuNPs into larger particles with desirable NIR adsorption in tumor site. Exploiting the bioorthogonal "Click and Release" (BCR) reaction between iminosydnone and cycloalkyne, aggregation of AuNPs can be achieved and attractively accompanied by the release of chemotherapeutic drug purposed to photothermal synergizing. We synthesize iminosydnone-lonidamine (ImLND) as a prodrug and choose dibenzocyclooctyne (DBCO) as the trigger of BCR reaction. A PEGylated AuNPs-based two-component nanoplatform consisting of prodrug-loaded AuNPs-ImLND and tumor-targeting peptide RGD-conjugated AuNPs-DBCO-RGD is designed. In the therapeutic regimen, AuNPs-DBCO-RGD are intravenously injected first for tumor-specific enrichment and retention. Once the arrival of AuNPs-ImLND injected later at tumor site, highly photothermally active nanoaggregates of AuNPs are formed via the BCR reaction between ImLND and DBCO. The simultaneous release of lonidamine further enhanced the therapeutic performance by sensitizing cancer cells to PTT.

Introduction

Cancer has been the most deadly disease in the majority of highly developed countries.[1] Recent statistics and analysis indicate that this range could expand to most countries around the world throughout this century.[2] The Global Cancer Observatory has made a shocking estimate that 13 million people will die from cancer each year by 2030.[3] As a disease with a complex pathological process, existing treatments including chemotherapy, radiotherapy, and surgery often encounter setbacks due to hazardous adverse effects and unsatisfactory therapeutic outcomes.[4] To address this issue, researchers have developed a range of novel therapeutic modalities, including but not limited to photodynamic therapy (PDT), chemodynamic therapy (CDT), photothermal therapy (PTT), and sonodynamic therapy (SDT). Therein, PTT utilizes the photothermal effect of photothermal agents (PTAs) under laser irradiation to induce the apoptosis of cancer cells or sensitize them to chemotherapy.[5] Due to the spatiotemporal controllability and noninvasiveness of PTT, unwanted damages to healthy tissues is significantly alleviated.[4c] Metal nanoparticles (MNPs) are among excellent PTAs due to their unique localized surface plasmon resonance (LSPR) behavior, which allows them to absorb and convert optical energy into heat through the Landau damping effect.[6] Among these MNPs, gold nanoparticles (AuNPs) attracted particular interest for their high biocompatibility and easily tunable morphology. However, there exists a dilemma occurs when the morphology and size of AuNPs are optimized for better PTT efficacy. Spherical AuNPs with smaller sizes (5–30 nm) are preferred for PTT due to their better blood biocompatibility and shorter biological half-life compared to the larger or differently shaped counterparts.[7] However, larger sizes of above 50 nm are required for desirable photothermal conversion under near-infrared (NIR) irradiation .[7b,c] To address this challenge, the transition of AuNPs from small spheres to larger aggregates with strong NIR absorption at the tumor site is highly desired. Researchers have exploited chemiluminescence-triggered click reactions,[7c] enzymatic condensation,[8] acidity-triggered charge reversal[9] and other tumor microenvironment (TME)-responsive reactions[10] to induce the aggregation of AuNPs upon their entry into tumor site. However, these approaches relied heavily on the biologically characteristics of the TME, which are often not as satisfactory as those established ex vivo by researchers. Additionally, AuNPs were used merely as PTAs, or the payload on AuNPs was not aimed at photothermal synergizing, which compromised the therapeutic outcome. More efforts are needed for more rational design of AuNP

[*] X. Yan,[+] K. Li,[+] T.-Q. Xie, X.-K. Jin, C. Zhang, Q.-R. Li, J. Feng, C.-J. Liu, X.-Z. Zhang
Key Laboratory of Biomedical Polymers of Ministry of Education & Department of Chemistry, Wuhan University, Wuhan 430072, P. R. China
E-mail: cjliu@whu.edu.cn
xz-zhang@whu.edu.cn
[+] These authors contributed equally to this work.

nanoagents to realize the "aggregation-induced photothermal activity" in tumor sites.

Given credit to the development of bioorthogonal chemistry, a unique subset of click chemistry has been discovered for facile conjugation of reactants under mild physiological environments without interfering with other biological processes, named bioorthogonal click chemistry.[11] Recently, effort has been devoted to the development of bioorthogonal "Click and Release" (BCR) reactions, in which unstable products are formed by click reactions and then quickly decompose to release molecular fragments. Representative BCR reactions are based on classic click reactions including the Staudinger reaction between azide and phosphine,[12] the inverse-electron-demand Diels–Alder reaction between tetrazine and trans-cyclooctene,[13] and the more recently specified [3+2] cycloaddition between mesoionic iminosydnone and cycloalkyne.[14] The "release" characteristic permits the design of cancer prodrugs and fluorophores, offering new ideas for developing targeted cancer theranostic.[13,15] Recently, a BCR reaction-based drug delivery system has entered phase 2 clinical trials,[16] highlighting the potential of BCR reactions for clinical application. Like click chemistry,[17] BCR reactions possess high reliability and selectivity with mild kinetics, which are suitable for the assembly of small spherical (<20 nm) AuNPs into photothermally active nanoaggregates in physiological milieu. What's more, the "release" characteristic can be utilized to release the attached drugs for synergistic combination of PTT with other therapeutic modalities.

Herein, we designed a two-component PEGylated AuNP-based nanoplatform for the enhanced tumor-targeted photothermal therapy. We employed a BCR reaction based on [3+2] cycloaddition between a mesoionic prodrug iminosydnone-lonidamine (ImLND) and dibenzocyclooctyne (DBCO) to form aggregates of AuNPs in vivo with the capability of releasing chemotherapeutic drug lonidamine (Scheme 1). Lonidamine provided the on-demand photothermal-synergistic ability in the design. By inhibiting aerobic glycolysis in cancerous cells, lonidamine can down-regulate the expression of heat shock proteins (HSP) that protect cells from hyperthermia-related damage,[18] thus

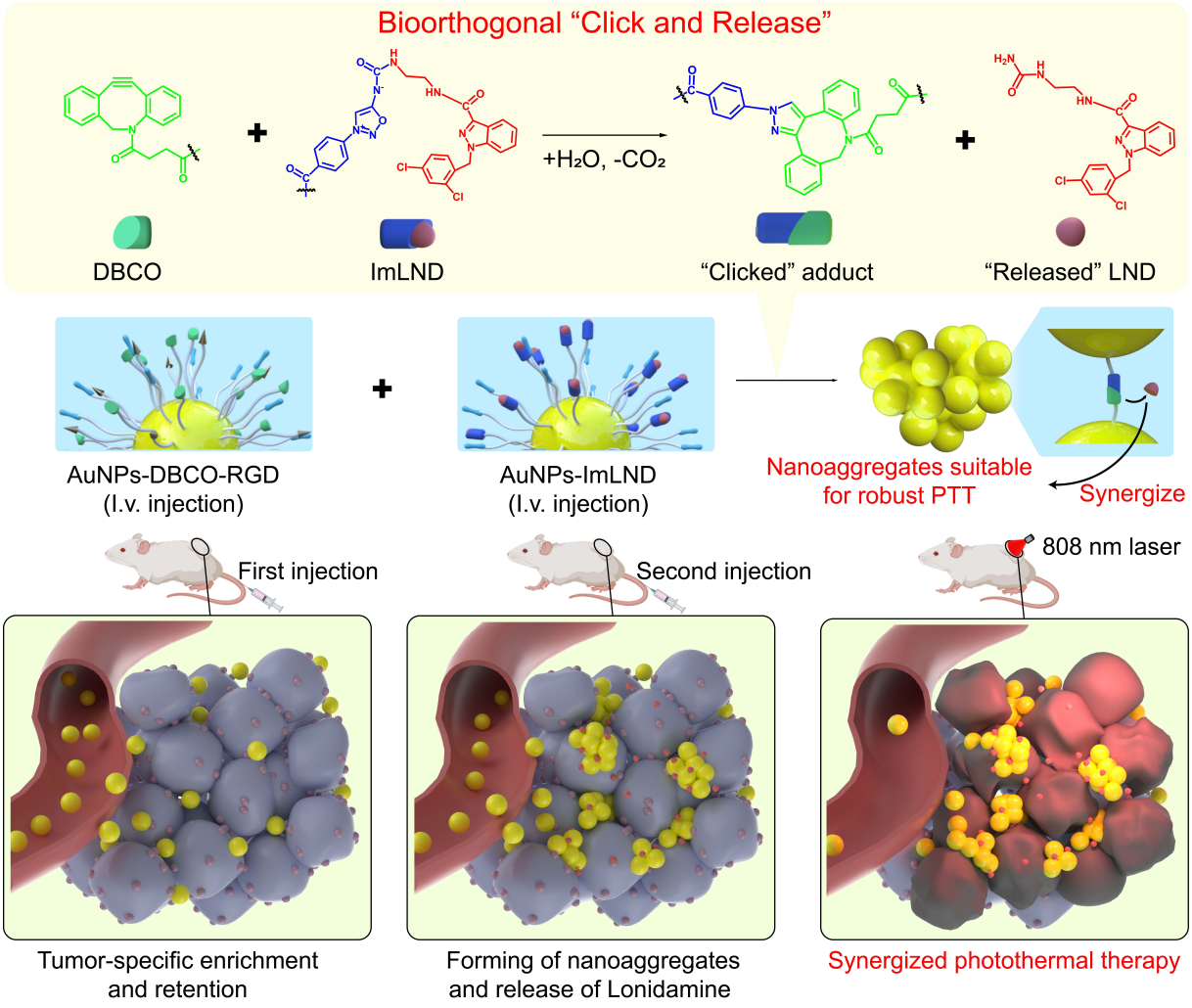

Scheme 1. Proposed therapeutic regimen of the two-component nanoplatform in this work.

enabling cancerous cells more sensitive to PTT. The nanoplatform consisted of two kinds of PEGylated AuNPs. One is the prodrug-loaded AuNPs-ImLND, the other is AuNPs-DBCO-RGD which acted as the trigger of BCR reaction and were modified with tumor targeting peptide RGD. The specific binding between RGD peptide and integrin $\alpha_v\beta_3$ overexpressed on the surface of tumor cells contribute to the tumor-targeting ability of AuNPs-DBCO-RGD.[19]

Considering the hydrophobicity of ImLND and DBCO, both AuNPs were further stabilized with sulfobetaine-based zwitterions to prevent premature aggregation during the period of blood circulation. In the therapeutic regimen, AuNPs-DBCO-RGD would be injected first for tumor-specific enrichment and retention. AuNPs-ImLND were injected later so that the off-target AuNPs-DBCO-RGD can be cleared to alleviate possible adverse effects. Upon the arrival of AuNPs-ImLND at tumor site, AuNPs-ImLND and AuNPs-DBCO-RGD would be crosslinked by BCR reaction to form larger aggregates with NIR absorption and release photothermal-synergistic lonidamine for enhanced PTT.

Results and Discussion

Preparation and characterization of AuNPs-ImLND and AuNPs-DBCO-RGD

AuNPs were prepared using the classic sodium citrate reduction method, and then PEGylated using HS-PEG_{5000}-NH_2 for further modifications, noted as AuNPs-NH_2 (Figure 1a). ImLND and a hydrophilic sulfobetaine-based zwitterion were introduced onto the surface of AuNPs-NH_2 through EDC/NHS-aided amide condensation to prepare drug-loaded AuNPs-ImLND. DBCO and zwitterion were introduced onto the surface of AuNPs-NH_2 using the same method to obtain AuNPs-DBCO. Then taking advantage of the azido-cycloalkyne click reaction, we synthesized and introduced N_3-RGD peptide (sequence: N_3-ARGD) to the surface of AuNPs-DBCO to prepare AuNPs-DBCO-RGD with tumor-targeting ability. A small portion of DBCO moieties (10 % approx.) was grafted with N_3-RGD peptide, which had negligible impact on the subsequent crosslink between the two species of AuNPs (Figure S14).

We conducted various characterizations to determine the physical property and chemical constitution of different AuNPs. The particle size distribution of the pristine AuNPs in the dry state was obtained by analyzing corresponding TEM images in ImageJ, which was then applied to nonlinear fit in GraphPad Prism 8 with a calculated diameter of 15.1 ± 1.3 nm (Figure 1b). The particle size distribution of AuNPs in dry state changed negligibly throughout the fabrication process (Figure S15). The hydrodynamic diameter of the AuNPs was measured using dynamic light scattering (DLS). The results showed that the number-weighted hydrodynamic diameter of AuNPs increased from 12 nm to 28 nm after PEGylation, and then decreased to 16 nm and 24 nm for AuNPs-ImLND and AuNPs-DBCO-RGD, respectively, due to the hydrophobicity of DBCO and ImLND (Figure 1c). The surface potential of AuNPs were also tested as it had close connections to the colloidal stability and biological clearance of AuNPs.[6b] Not surprisingly, pristine AuNPs prepared by citrate reduction possessed a highly negative surface potential of −22 mV, which then reversed to a positive one of 17 mV due to the primary amine group introduced by PEGylation (Figure 1d). The Zeta potentials of AuNPs reversed to negative ones again because the introduction of sulfobetaine-based zwitterion left the surface

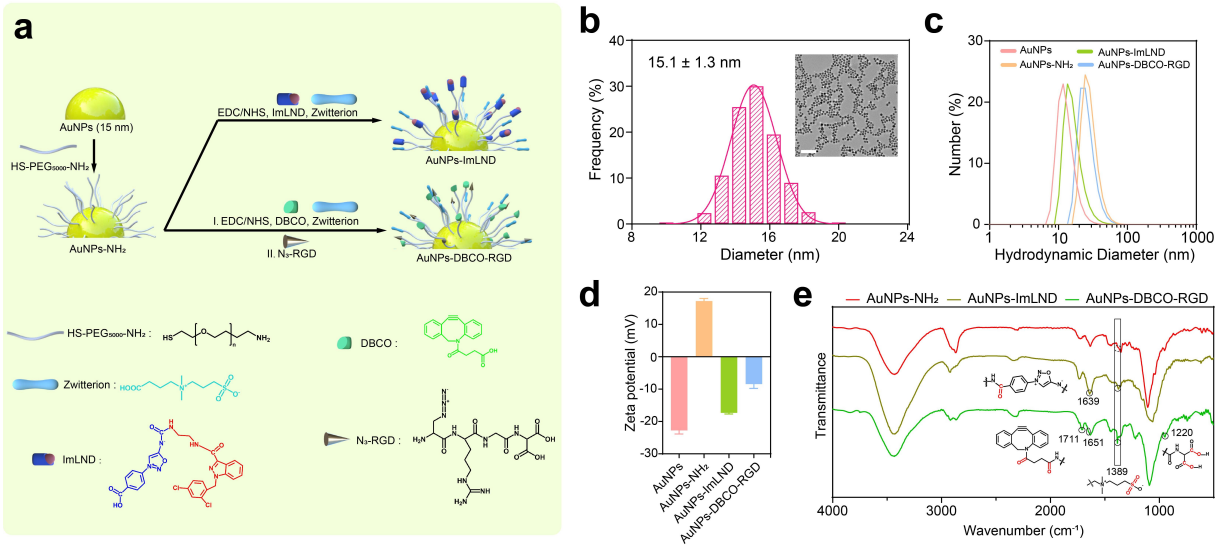

Figure 1. Fabrication and characterization of the PEGylated AuNPs-based nanoplatform. (a) Fabrication of AuNPs-ImLND and AuNPs-DBCO-RGD. (b) Particle size distribution of AuNPs used in this work. (inset: TEM images of AuNPs, scale bar 100 nm) (c) Number weighted hydrodynamic diameter of different AuNPs. (d) Surface potential of different AuNPs (data are shown as mean with SD, $n=3$). (e) FT-IR spectra of different AuNPs.

of AuNPs with negatively charged sulfonic groups. A negative surface potential is preferable for in vivo application as unwanted absorption or adhesion is less likely to occur between AuNPs and biological objects. We estimated that the surface of AuNPs-ImLND had a higher density of zwitterionic moieties than AuNPs-DBCO-RGD, as their zeta potential was measured to be −17 mV and −8 mV, respectively (Figure 1d). FT-IR tests were carried out to qualitatively confirm the introduction of functional moieties The absorption peak at 1389 cm^{-1} in the olivine and green curve corresponded to the sulfonic group in zwitterionic moiety (Figure 1e). Meanwhile, the absorption peak at 1639 cm^{-1} in olivine curve and ones at 1711 cm^{-1}, 1651 cm^{-1} in green curve corresponded to carbonyl groups in ImLND and DBCO. Additionally, the absorption peak at 1220 cm^{-1} corresponded to the carboxyl groups of aspartic acid residue in RGD peptide. The results of FT-IR test confirmed the successful preparation of AuNPs-ImLND and AuNPs-DBCO-RGD.

The residual solutions from the step of EDC/NHS-aided amide condensation were analyzed by HPLC to quantitatively confirm the introduction of functional moieties on AuNPs (Figure S16). The loading capacity was calculated as 2.20 μg ImLND/μg Au and 1.15 μg zwitterion/μg Au for AuNPs-ImLND, and 1.76 μg DBCO/μg Au and 0.75 μg zwitterion/μg Au for AuNPs-DBCO-RGD. The results of quantitative characterization confirmed our estimation that AuNPs-ImLND packed more zwitterionic moieties on surface than AuNPs-DBCO-RGD.

BCR reaction triggered aggregation of AuNPs and drug release

After successful preparation of the two-component nanoplatform, we carried out in vitro testing of the BCR reaction-triggered chemical crosslinking of AuNPs and the release of lonidamine (Figure 2a). The colloidal stability of AuNPs was tested to exclude any interference from possible intrinsic aggregation behavior of AuNPs (Figure S17). To simulate physiological conditions, the two kinds of AuNPs were suspended in PBS (pH 7.4) and mixed in a DLS testing cell, then kept in a 37 °C shaker for the BCR reaction to occur. Reaction mixtures at different time points were sampled and quenched with a solution of excessive PEG_{550}-N_3 for TEM observation on the aggregation behavior of AuNPs. The supernatants of the reaction mixture after reacting for 24 h were collected for HPLC/LC–MS analysis of the released lonidamine. We also conducted DLS and UV/Vis study to confirm the alteration in hydrodynamic size and optical absorbance properties of the reaction mixture. As shown in the results (Figure 2b), small aggregates with a hydrodynamic size of 200 nm were observed 4 h after the reaction started, but corresponding UV/Vis spectra exhibited negligible change compared to initial state in the NIR region (750–1100 nm) indicating unaltered LSPR property. After 8 h of the reaction, the color of the reaction mixture turned dark and middle-sized aggregates with hydrodynamic diameter of 800 nm were observed in TEM image. Obvious absorbance in the NIR region of UV/Vis spectra was also confirmed, indicating the alteration in LSPR property. Then, after reacting for 12 h, massive aggregates with hydrodynamic size over 1000 nm were observed, precipitates were generated on the bottom of the cell, leading to decreased overall absorbance in UV/Vis spectra but the tendency of relative high absorbance in the NIR region was preserved. More precipitates were generated after reacting for 24 h, resulting in further decreased overall absorbance but preserved relatively high NIR absorbance in the UV/Vis spectra. As control, we quenched the reactive DBCO moieties on surface of AuNPs-DBCO-RGD with excessive PEG_{550}-N_3 to form triazole, such AuNPs were named AuNPs-TRZO-RGD. We performed the same tests on a

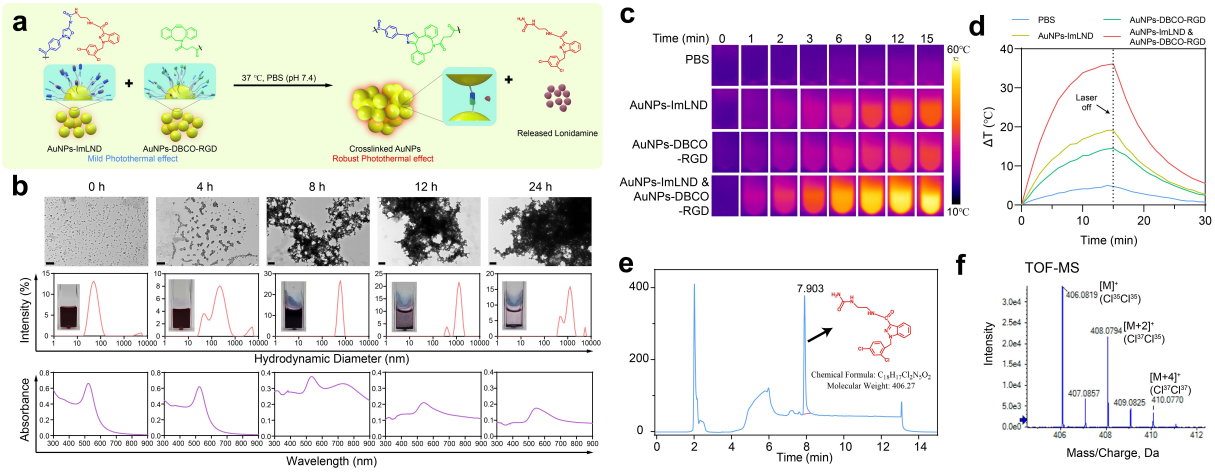

Figure 2. (a) Schematic illustration of BCR reaction-triggered aggregation of AuNPs and drug release. (b) TEM images (scale bar: 200 nm), intensity weighted hydrodynamic diameter and UV/Vis absorption curve of the reaction mixture containing equivalent AuNPs-ImLND and AuNPs-DBCO-RGD (total concentration of Au: 0.6 mg/mL) at different time points. (c) Thermal images of PBS, AuNPs-ImLND and AuNPs-DBCO-RGD and aggregated AuNPs irradiated by 808 nm laser at different time points. (d) ΔT-Time curve of thermal images. (e) HPLC results of the supernatants from suspension of aggregated AuNPs and (f) corresponding liquid chromatography-mass spectrum (LC–MS) results.

mixture of AuNPs-TRZO-RGD and AuNPs-ImLND (total concentration of Au: 0.6 mg/mL). No obvious aggregation was observed in TEM images across the experimental timeline (Figure S18). Intensity weighted hydrodynamic diameter and absorbance property of the colloidal solution also exhibited negligible alteration (Figure S18). As the sole altered variable between the two sets of experiments was the reactivity of DBCO moieties, the distinctive aggregation behavior of AuNPs in group with reactive DBCO moieties could be attributed to the occurrence of BCR reaction.

After confirming the BCR reaction-triggered aggregation behavior of AuNPs, we studied the proposed photothermal enhancement effect. The two kinds of AuNPs were mixed and reacted in a 37 °C shaker for 8 h, and then quenched by excessive PEG_{550}-N_3 to obtain a suspension of aggregated AuNPs with minimum precipitation and highest absorbance in NIR region. PBS solution of AuNPs-ImLND and AuNPs-DBCO-RGD alone was also tested for their photothermal effect to distinguish the enhancement of crosslinked AuNPs, and pure PBS was tested as blank control. All samples were loaded into an uncapped 5 mL centrifuge tube and then radiated by 808 nm laser with a power density of 1.25 W/cm^2 from directly above for 15 min. Thermal images were taken horizontally from the right with an infrared camera. As shown in the results (Figure 2c, d), the two kinds of AuNPs alone possessed mild photothermal effect comparing to PBS. However, aggregated AuNPs exhibited prominent photothermal effect, with a calculated photothermal conversion rate of 53.7 %. The photothermal stability of the nanoaggregates were also investigated to exclude possible disassembly caused by high temperature (Figure S19). The relation between concentration of Au and photothermal enhancement effect (Figure S20) and the aggregation-activated PAI activity was also investigated for further experiments (Figure S21).

To confirm the release of lonidamine by BCR reaction, the supernatants from suspension of aggregated AuNPs were collected and subjected to HPLC and LC–MS tests. An absorption peak at an elution time of 7.903 min was distinguished from the HPLC results (Figure 2e). A molecular ion peak of released lonidamine was observed in corresponding LC–MS results at m/z = 406.0819 (Figure 2f). As lonidamine possessed two chloride atoms, a characteristic ratio of isotopic relative abundance of M: M + 2: M + 4 = 9: 6: 1 was also observed in mass spectrum. The release profile of lonidamine was also investigated by performing HPLC tests on ultrafiltrate of the reaction mixture at different time points (Figure S22). The cumulative release rete of lonidamine in 24 h was calculated as 78.6 %.

The results of the photothermal enhancement study verified that the BCR reaction can trigger aggregation of AuNPs with mild kinetic, providing on-demand absorbance in NIR region crucial for robust PTT. The release of the chemotherapeutic drug lonidamine was also confirmed by HPLC and LC–MS, making synergized PTT possible. We also evaluated the colloidal stability and the reactivity of AuNPs in serum (Figure S23, S24) to further confirm the feasibility of triggering BCR reaction in vivo.

Biocompatibility tests and synergized photothermal ablation of cancer cells

We carried out biocompatibility tests on the two kinds of AuNPs to prepare for the in vivo application of the two-component nanoplatform. The murine embryonic 3T3 cell line was extensively used for the validation of biocompatibility for nanomaterials. We incubated 3T3 cells with a serial dilution of different AuNPs (0.1, 0.2, 0.3, 0.4, 0.6, 0.8, 1 mg/mL) for 24 h, and a MTT test was performed to determine the cell viability after the incubation. Both kinds of AuNPs remained biocompatibility with a concentration no higher than 0.6 mg/mL as cell viability was maintained over 80 % (Figure 3a). When the concentration of Au exceeded 0.8 mg/mL, observable cytotoxicity was observed in cells incubated with AuNPs-DBCO-RGD (Figure 3a). This result could be attributed to the cytotoxicity of RGD peptide, as reported previously.[19] As the proposed method of administration was intravenous injection, hemolysis tests were also conducted on both kinds of AuNPs with freshly extracted red blood cells form female Balb/C mice. According to the results, the hemolysis rate of both kinds of AuNPs were kept under 3 % with a concentration no higher than 0.8 mg/mL (Figure 3b). Observable hemolysis was provoked by 1 mg/mL AuNPs of both kinds, while AuNPs-ImLND causes slightly severer hemolysis than AuNPs-DBCO-RGD (Figure 3b). We supposed this result was due to the higher density of zwitterion on the surface of AuNPs-ImLND, as high concentration of zwitterion may disrupt the integrity of cellular membrane.

To test the synergized PTT of the two-component nanoplatform, we carried out photothermal ablation of murine breast cancer cell line 4T1 in vitro. 4T1 cells were seeded in 24-well and 6-well plate and incubated with a mixture of equivalent AuNPs-ImLND and AuNPs-DBCO-RGD (total concentration of Au: 0.3 mg/mL) for 12 h to let the BCR reaction occur. Then the plate was irradiated by 808 nm laser (1.25 W/cm^2) for 5 min. The MTT tests and live-dead staining were performed 12 h later. As shown in the results, AuNPs-ImLND and AuNPs-DBCO-RGD alone exhibited minor cytotoxicity against 4T1 cells without irradiation of 808 nm laser (Figure 3c), and several PI-stained dead cells with red fluorescence could be distinguished in live-dead staining images (Figure 3d). The mixture of the two kinds of AuNPs exhibited mild cytotoxicity against 4T1 cells due to the release of lonidamine by BCR reaction (Figure 3c). With the irradiation of 808 nm laser, visible cytotoxicity was observed in cells treated with AuNPs-ImLND or AuNPs-DBCO-RGD, as a small portion of dead cells were observed in live-dead staining images (Figure 3d). While significant cytotoxicity was observed in group treated with a mixture of AuNPs-ImLND and AuNPs-DBCO-RGD (Figure 3c, d), due to the robust photothermal effect of aggregated AuNPs and the synergistic release of lonidamine. The Western-blotting tests were carried out to further confirm the photothermal-synergizing effect of lonidamine by downregulating HSP (Figure S25). We also collected cells from all groups for Bio-TEM tests to visually confirm the aggregation of AuNPs (Figure 3e).

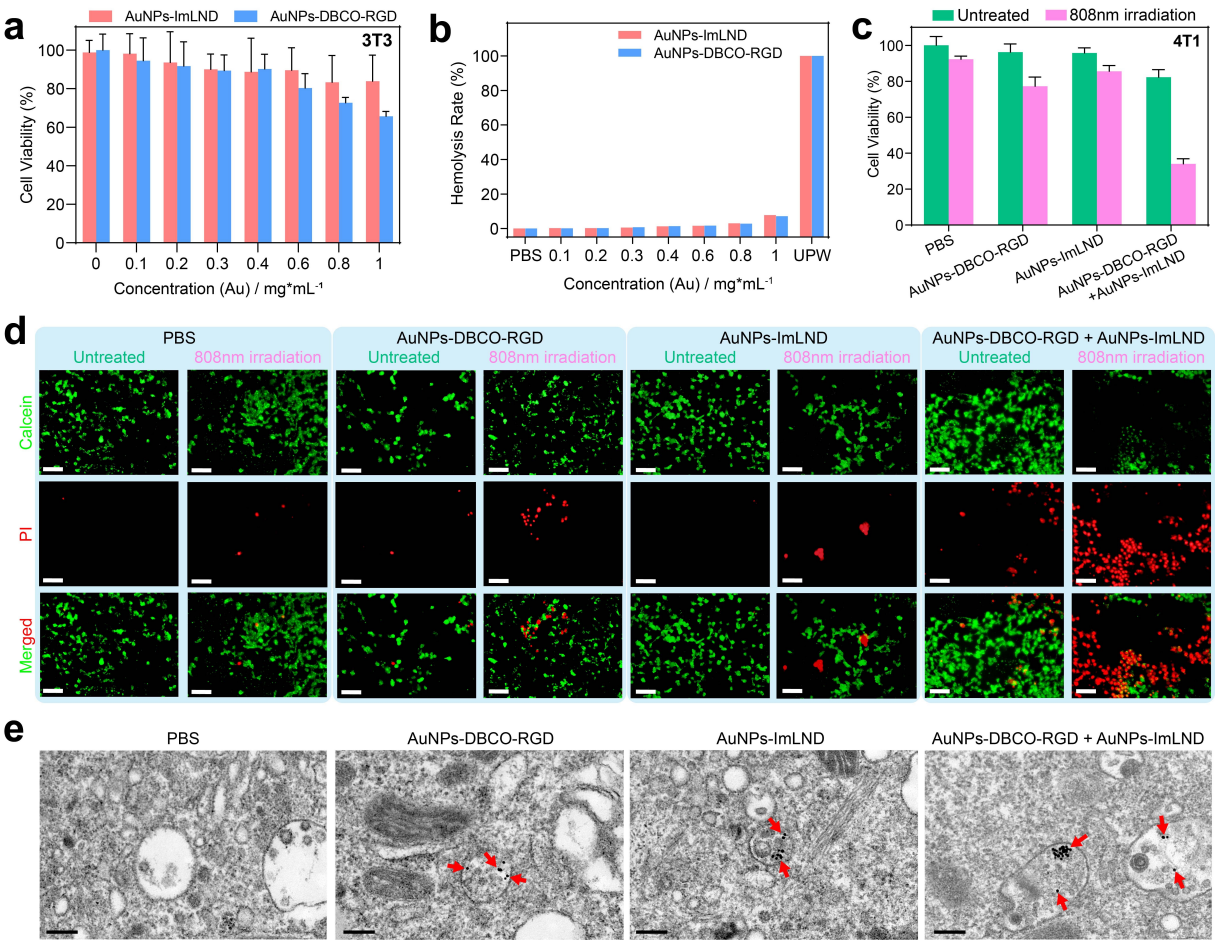

Figure 3. Biocompatibility tests of AuNPs and photothermal ablation of cancer cells in vitro. (a) Cell viability assay results after incubating a serial dilution of AuNPs with murine embryonic 3T3 cells for 24 h (data are shown as mean with SD, $n=5$). (b) Hemolysis assay of AuNPs on fresh red blood cell extracted from healthy female Balb/C mice. (c) Cell viability assay results after photothermal ablation of murine breast cancer cell line 4T1 (data are shown as mean with SD, $n=5$). (d) Live-dead staining images after photothermal ablation of murine 4T1 cells (scale bar: 100 μm). (e) Representative Bio-TEM images of 4T1 cells incubated with different AuNPs (scale bar: 200 nm), AuNPs were indicated by red arrows.

Images of cells from PBS group were taken as blank control to exclude possible mistaking of cellular components as AuNPs. As shown in Bio-TEM images of cells incubated with sole AuNPs-DBCO-RGD and AuNPs-ImLND, only discrete AuNPs were found intracellularly. But in image of cells incubated with combination of AuNPs-DBCO-RGD and AuNPs-ImLND, nanoaggregate of AuNPs could be distinguished besides discrete AuNPs intracellularly. Visual confirmation on the forming of nanoaggregates bore out the intracellular occurrence of BCR reaction. The confocal laser scanning microscope was also exploited to visualize the intracellular presence of nanoaggregates (Figure S26).

Biocompatibility tests and hemolysis assay on AuNPs used as experimental counterparts were also conducted to confirm their biosafety for further in vivo experiments (Figure S27).

We have confirmed the biocompatibility of the two-component nanoplatform and the synergized PTT effect against murine breast cancer 4T1 cell line in vitro, achieving the preliminary preparation for the application of the nanoplatform in vivo.

RGD-based tumor targeting and BCR reaction-triggered aggregation of AuNPs in vivo

After confirming the biocompatibility and synergistic PTT ability of the nanoplatform in vitro, we further carried out in vivo studies on the tumor-targeting, PTT and PAI abilities of the nanoplatform. In our proposed therapeutic regimen, two key points were crucial for realizing synergized tumor targeting PTT: 1) RGD-based tumor-specific enrichment and retention of AuNPs-DBCO-RGD, and 2) the BCR reaction between ImLND and DBCO triggered aggregation of AuNPs, i.e., the retention of AuNPs-ImLND at tumor site due to the formation of nanoaggregates. To testify this, we established 4 groups based on two variants: the conjugation of RGD peptide and the reactivity of DBCO moieties, denoted as AuNPs-DBCO, AuNPs-TRZO, AuNPs-DBCO-RGD and AuNPs-TRZO-RGD (Figure 4a). AuNPs-DBCO is the precursor of AuNPs-DBCO-RGD before further conjugation with N_3-RGD peptide. The reactive DBCO groups on surface of AuNPs-TRZO and AuNPs-TRZO-RGD were quenched with PEG_{550}-N_3 to

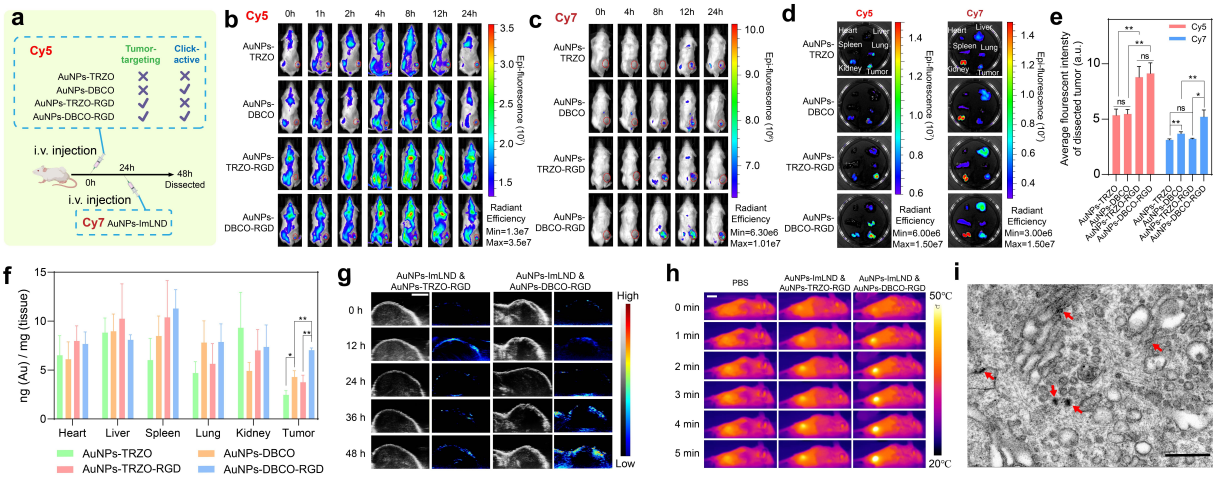

Figure 4. (a) Schematic illustration of the study on tumor-targeting ability of the two-component nanoplatform. (b) In vivo fluorescent images of mice injected with Cy5 labelled AuNPs-DBCO-RGD or its experimental counterparts. (c) In vivo fluorescent images of mice injected with Cy7 labelled AuNPs-ImLND. (d) Fluorescent images of dissected organs. (e) Results of quantitative analysis of fluorescent intensity on dissected tumor (data are shown as mean with SD, $n=5$. *: $P<0.05$, **: $P<0.01$, ns: no statistical significance). (f) Biodistribution of Au in major organs and tumor after the experiment (data are shown as mean with SD, $n=5$. *: $P<0.05$, **: $P<0.01$). (g) Ultrasonic and photoacoustic image of tumor (Scale bar: 8 mm). (h) Thermal images of mice receiving irradiation of 808 nm laser (1.25 W/cm^2) after different treatment (Scale bar: 1 cm). (i) Representative Bio-TEM image of tumor tissue slices from mice treated with AuNPs-DBCO-RGD/AuNPs-ImLND (scale bar: 500 nm), red arrows indicate presence of AuNPs. Unit of the radiant efficiency in (b), (c), (d) is $(\frac{p/sec/cm^2/sr}{\mu W/cm^2})$ according to the IVIS system.

form unreactive triazole, such AuNPs were unable to trigger BCR reaction. Mouse breast cancer cell 4T1 was subcutaneously injected on the dorsal side of healthy female Balb/C mice to establish mouse tumor model. Tumor-bearing mice were intravenously injected with a first does of 0.2 mL Cy5 labeled AuNPs-DBCO-RGD (0.6 mg Au/mL) or its experimental counterparts to study the RGD-based tumor targeting ability. In vivo fluorescent images were taken at different time points after injection. Stronger fluorescent signals on tumor site of Cy5 were observed from in vivo fluorescent images of the "AuNPs-DBCO-RGD" and "AuNPs-TRZO-RGD" groups than their none-RGD-conjugated counterparts over the entire experimental timeline (Figure 4b). The distinct difference between signal intensities indicated that AuNPs conjugated with RGD peptide possessed better tumor-specific enrichment and retention. Afterwards, we intravenously injected a second dose of 0.2 mL Cy7 labeled AuNPs-ImLND (0.6 mg Au/mL) 24 h after the first dose to study its BCR reaction-based tumor retention behavior. The overall fluorescent intensity of Cy7 was weaker than that of Cy5. This is probably due to the lower reaction activity of Cy7-NHS, which led to less Cy7 conjugation on the surface of AuNPs-ImLND. While the strongest signal of Cy7 was observed form the in vivo fluorescent images of the "AuNPs-DBCO-RGD" group due to the higher enrichment of the first dose of AuNPs and the preserved reactivity of the DBCO moieties (Figure 4c). AuNPs-DBCO also possessed reactive DBCO moieties but failed to cause a significant enhancement in the retention of AuNPs-ImLND due to the lack of tumor-specific enrichment and retention ability. All mice were executed 24 h after injection of AuNPs-ImLND, major organs and tumors were dissected and applied to fluorescent imaging. The fluorescent intensity of dissected tumors was quantitatively analyzed. Higher signal intensity of Cy5 were observed in the dissected tumors compared to other major organs in all groups. Comparable mild fluorescent signals were observed in the kidney, lung, and liver, while no visible fluorescent signals were observed in the heart or spleen, indicating near-complete clearance of off-target AuNPs of the first dose (Figure 4d). We performed detailed investigation on the concentration of AuNPs-DBCO-RGD (Figure S28), from which a biological half-life of 4 h was concluded. The clearance of off-target AuNPs-DBCO-RGD was also confirmed as the concentration of Au in blood and major organs dropped significantly 24 hours after the injection. A quantitative analysis of the fluorescent intensity of Cy5 in dissected tumors showed statistically significant difference between RGD-conjugated AuNPs and their non-RGD-conjugated counterparts, further confirming the tumor targeting and retention mediated by RGD ligands (Figure 4e). In terms of the distribution of Cy7 fluorescence, which indicates the presence of AuNPs-ImLND, strong signals were observed in the kidneys of all groups, indicating possible renal clearance of the injected AuNPs-ImLND (Figure 4d). Comparable fluorescent signals on livers and spleens indicated capture of AuNPs-ImLND by the reticulum endothelium system (RES). A quantitative analysis of the fluorescent intensity of Cy7 on dissected tumors revealed statistically significant difference between the group with reactive DBCO moieties and their DBCO-quenched counterparts due to the enhanced retention of AuNPs-ImLND mediated by BCR reactions (Figure 4e). However, no significant difference was observed between the two DBCO-quenched groups as they were unable to trigger BCR reactions. Additionally, statistical difference was found between the "AuNPs-DBCO" and "AuNPs-

DBCO-RGD" groups as the latter had better tumor-specific enrichment for the first dose of AuNPs. To further map the biodistribution of Au after two doses of AuNPs, organs and tumor were digested with a mixture of nitric acid and hydrogen peroxide for ICP-MS testing. The distribution of Au among intact organs indicated that liver and spleen, as part of the RES, took up the majority of the AuNPs (Figure S29). However, after normalizing the results by the unit weight of tissues, the distribution of Au exhibited a more averaged pattern (Figure 4f). Statistical analysis was performed on the proportion of Au in the tumor from all groups, and the results were consistent with those drawn from fluorescent imaging tests. The highest proportion was observed in the "AuNPs-DBCO-RGD" group as both doses of AuNPs had better retention.

We performed PAI and PTT experiments to further confirm the BCR reaction-triggered aggregation of AuNPs in tumor. Two doses of AuNPs (AuNPs-DBCO-RGD or AuNPs-TRZO-RGD, followed by AuNPs-ImLND) were sequentially injected into tumor bearing mice according to the same regimen in tumor-targeting experiment. Intriguingly, a stronger photoacoustic (PA) signal was observed from group treated by AuNPs-TRZO-RGD on 12 h. We assumed this was probably a result of quenched hydrophobic DBCO moieties with PEG_{550}-N_3. Leading to higher hydrophilicity of AuNPs-TRZO-RGD thus faster pharmacokinetic performance. Eventually rendered AuNPs-TRZO-RGD to accumulate faster than AuNPs-DBCO-RGD in the tumor. But still an obviously stronger PA signal was observed from group treated with AuNPs-DBCO-RGD/AuNPs-ImLND 48 hours after the first dosage, due to the aggregation of AuNPs caused by BCR reaction (Figure 4g). After taking photoacoustic images 48 h after the first dose of AuNPs, mice were immediately subjected to PTT with 808 nm laser irradiation on tumor site. Thermal images obtained showed prominent photothermal enhancement in the group treated with AuNPs-DBCO-RGD and AuNPs-ImLND (Figure 4h), further confirming the generation of nanoaggregates by BCR reaction in the tumor site. Visual confirmation of aggregated AuNPs was also made in a similar way with in vitro experiments. Tumor tissues from mice treated with AuNPs-TRZO-RGD/AuNPs-ImLND or AuNPs-DBCO- RGD/AuNPs-ImLND were dissected and applied to slice and Bio-TEM tests. Discrete AuNPs and nanoaggregates were both observed in Bio-TEM image of group treated with AuNPs-DBCO-RGD/AuNPs-ImLND (Figure 4i). While comparable nanoaggregates were absent in Bio-TEM image of group treated with AuNPs-TRZO-RGD/AuNPs-ImLND (Figure S30).

We verified the RGD-based tumor-targeting ability of AuNPs-DBCO-RGD and the BCR reaction triggered retention of AuNPs-ImLND, as well as the formation of nanoaggregates in vivo. Our results have also proven the feasibility of our proposed therapeutic regimen in enhancing cancer PTT based on this nanoplatform.

BCR reaction-enhanced PTT of mice tumor model

After confirming the feasibility of employing nanoplatform in vivo for enhanced PTT, we conducted tests on its therapeutic effect on a mouse tumor model. Tumor-bearing mice were divided into 6 groups and treated according to our earlier proposed therapeutic regimen (Figure 5a). Tumor volume and body weight of mice from all groups were monitored and recorded every 2 days (Figure 5b, c). On the 24th day of the experiment, blood samples were taken from mice in all groups for full blood count and blood biochemistry tests. Then all mice were euthanized and dissected, major organs and tumor were embedded in paraffin and sliced for H&E staining. Photographs of the dissected tumors from all groups were taken (Figure 5d). As shown in the tumor volume-time plot (Figure 5b) and photograph of dissected tumors (Figure 5d), only the "DBCO-RGD + ImLND + 808 nm" group achieved prominent suppression of tumor growth, and even complete tumor regression due to the triggering of BCR reaction. The aggregated AuNPs and released lonidamine boosted the therapeutic effect of PTT, leading to a robust tumor suppression effect in the "DBCO-RGD + ImLND + 808 nm"

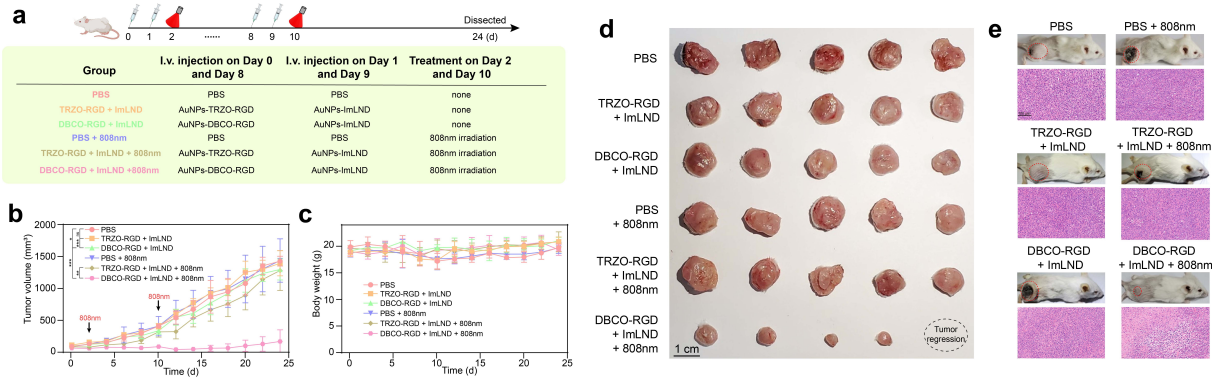

Figure 5. (a) Therapeutic regimen of the nanoplatform for enhanced PTT on mice tumor model. (b) Tumor volume of mice from different groups (data are shown as mean with SD, $n = 5$. *: $P < 0.05$, **: $P < 0.01$, ***: $P < 0.001$, ns: no statistical significance). (c) Body weight of mice from different groups (data are shown as mean with SD, $n = 5$.). (d) Photograph of dissected tumors from different groups after the experiment (scale bar: 1 cm). (e) Representative photos of mice from different groups and corresponding H&E staining images of tumor (scale bar: 100 μm).

group. In contrast, only minor suppression of tumor was observed in the "TRZO-RGD + ImLND + 808 nm" group, which was attributed to the mild photothermal effect of unaggregated AuNPs. The elimination of reactive DBCO moieties prevented the occurrence of BCR reaction, resulting in a limited therapeutic effect. Minor suppression effect was also observed in the "DBCO-RGD + ImLND" group as the released lonidamine alone can only slightly suppress the growth of cancerous cells, consistent with the results of in vitro experiments on cancer cells. Densely packed malignant tumor tissue was observed in H&E staining images of tumors from all groups except the "DBCO-RGD + ImLND" group (Figure 5e), further indicating the remarkable PTT effect of the nanoplatform in vivo.

The biocompatibility of the nanoplatform was also further verified in the PTT experiment. The body weight of the mice fluctuated within normal range throughout the therapeutic process (Figure 5c). No palpable lesions were observed in post-therapy H&E staining images of major organs in all groups (Figure S31). Results of post-therapy blood biochemistry tests and full blood count demonstrated no obvious deviation from normal ranges (Figure S32, S33).

Conclusion

Taking advantage of the iminosydnone-dibenzocyclooctyne BCR reaction, we successfully developed a biocompatible nanoplatform consisting of prodrug-loaded AuNPs-ImLND and AuNPs-DBCO-RGD as BCR reaction trigger. AuNPs-DBCO-RGD were intravenously injected first for its RGD peptide-endowed tumor-specific targeting and retention. AuNPs-ImLND were injected later for the forming of nanoaggregates and the release of lonidamine at tumor site. The formation of nanoaggregates through the BCR reaction leads to the activation of strong photothermal and photoacoustic activity, which was confirmed both in vitro and in vivo. Photothermal ablation of cancer cells in vitro confirms the synergistic effect between nanoaggregates-based PTT and released lonidamine. In vivo experiment on a mouse tumor model further confirmed the biocompatibility and robust PTT effect of the nanoplatform. Our work utilizes both the "Click" and "Release" components of the BCR reaction to optimize the therapeutic outcomes of PTT. We believe that more applications for the BCR reaction await discovery in the vast field of biomedicine.

Supporting Information

The authors have cited additional references within the Supporting Information.[14,20]

Acknowledgements

This work was supported by the National Natural Science Foundation of China (52373304, 52073219, 22135005, 51833007). We thank the support from the Large-scale Instrument and Equipment Sharing Foundation of Wuhan University. All animal studies were approved by the Institutional Animal Care and Use Committee (IACUC) of the Animal Experiment Center of Wuhan University (Wuhan, P. R. China) (WP20210503).

Conflict of Interest

The authors declare no conflict of interest.

Data Availability Statement

The data that support the findings of this study are available from the corresponding author upon reasonable request.

Keywords: Click chemistry · Bioorthogonal chemistry · Gold nanoparticle · Photothermal therapy · Synergistic therapy

[1] a) R. L. Siegel, K. D. Miller, N. S. Wagle, A. Jemal, *Ca-Cancer J. Clin.* **2023**, *73*, 17–48; b) C. Xia, X. Dong, H. Li, M. Cao, D. Sun, S. He, F. Yang, X. Yan, S. Zhang, N. Li, W. Chen, *Chin Med J (Engl)* **2022**, *135*, 584–590.
[2] F. Bray, M. Laversanne, E. Weiderpass, I. Soerjomataram, *Cancer* **2021**, *127*, 3029–3030.
[3] T. Lancet, *Lancet* **2018**, *392*, 985.
[4] a) A. Kalbasi, C. Komar, G. M. Tooker, M. Liu, J. W. Lee, W. L. Gladney, E. Ben-Josef, G. L. Beatty, *Clin. Cancer Res.* **2017**, *23*, 137–148; b) N. J. Curtin, *Nat. Rev. Cancer* **2012**, *12*, 801–817; c) Y. Liu, P. Bhattarai, Z. Dai, X. Chen, *Chem. Soc. Rev.* **2019**, *48*, 2053–2108; d) I. de Lazaro, D. J. Mooney, *Nat. Mater.* **2021**, *20*, 1469–1479.
[5] a) C. Xu, K. Pu, *Chem. Soc. Rev.* **2021**, *50*, 1111–1137; b) Y. Jiang, J. Huang, C. Xu, K. Pu, *Nat. Commun.* **2021**, *12*, 742.
[6] a) S. Palani, J. P. Kenison, S. Sabuncu, T. Huang, F. Civitci, S. Esener, X. Nan, *ACS Nano* **2023**, *17*, 2266–2278; b) N. Khlebtsov, L. Dykman, *Chem. Soc. Rev.* **2011**, *40*, 1647–1671.
[7] a) Y. Wu, Y. He, M. Han, D. Zhao, B. Liu, K. Yuan, H. Sun, H.-M. Meng, Z. Li, *CCS Chemistry* **2023**, *5*, 1561–1573; b) P. Huang, J. Lin, W. Li, P. Rong, Z. Wang, S. Wang, X. Wang, X. Sun, M. Aronova, G. Niu, R. D. Leapman, Z. Nie, X. Chen, *Angew. Chem. Int. Ed. Engl.* **2013**, *52*, 13958–13964; c) Q. Mao, J. Fang, A. Wang, Y. Zhang, C. Cui, S. Ye, Y. Zhao, Y. Feng, J. Li, H. Shi, *Angew. Chem. Int. Ed. Engl.* **2021**, *60*, 23805–23811.
[8] J. Chen, Y. Ma, W. Du, T. Dai, Y. Wang, W. Jiang, Y. Wan, Y. Wang, G. Liang, G. Wang, *Adv. Funct. Mater.* **2020**, *30*.
[9] S. Luan, R. Xie, Y. Yang, X. Xiao, J. Zhou, X. Li, P. Fang, X. Zeng, X. Yu, M. Chen, H. Gao, Y. Yuan, *Small* **2022**, *18*, e2200115.
[10] D. Liu, L. Liu, F. Liu, M. Zhang, P. Wei, T. Yi, *Adv. Sci.* **2021**, *8*, e2100074.
[11] a) D. Wu, K. Yang, Z. Zhang, Y. Feng, L. Rao, X. Chen, G. Yu, *Chem. Soc. Rev.* **2022**, *51*, 1336–1376; b) E. M. Sletten, C. R. Bertozzi, *Angew. Chem. Int. Ed. Engl.* **2009**, *48*, 6974–6998.
[12] M. Azoulay, G. Tuffin, W. Sallem, J. C. Florent, *Bioorg. Med. Chem. Lett.* **2006**, *16*, 3147–3149.
[13] R. M. Versteegen, R. Rossin, W. ten Hoeve, H. M. Janssen, M. S. Robillard, *Angew. Chem. Int. Ed. Engl.* **2013**, *52*, 14112–14116.

[14] S. Bernard, D. Audisio, M. Riomet, S. Bregant, A. Sallustrau, L. Plougastel, E. Decuypere, S. Gabillet, R. A. Kumar, J. Elyian, M. N. Trinh, O. Koniev, A. Wagner, S. Kolodych, F. Taran, *Angew. Chem. Int. Ed. Engl.* **2017**, *56*, 15612–15616.
[15] a) R. Rossin, S. M. van Duijnhoven, W. Ten Hoeve, H. M. Janssen, L. H. Kleijn, F. J. Hoeben, R. M. Versteegen, M. S. Robillard, *Bioconjugate Chem.* **2016**, *27*, 1697–1706; b) K. Porte, B. Renoux, E. Peraudeau, J. Clarhaut, B. Eddhif, P. Poinot, E. Gravel, E. Doris, A. Wijkhuisen, D. Audisio, S. Papot, F. Taran, *Angew. Chem. Int. Ed. Engl.* **2019**, *58*, 6366–6370.
[16] M. Peplow, *Nat. Biotechnol.* **2023**, *41*, 883–885.
[17] a) H. C. Kolb, M. G. Finn, K. B. Sharpless, *Angew. Chem. Int. Ed.* **2001**, *40*, 2004–2021; b) P. L. Golas, K. Matyjaszewski, *Chem. Soc. Rev.* **2010**, *39*, 1338–1354; c) S. A. Fisher, A. E. G. Baker, M. S. Shoichet, *J. Am. Chem. Soc.* **2017**, *139*, 7416–7427; d) D. Astruc, L. Liang, A. Rapakousiou, J. Ruiz, *Acc. Chem. Res.* **2012**, *45*, 630–640; e) S. Shi, Z. Wang, Y. Deng, F. Tian, Q. Wu, P. Zheng, *CCS Chemistry* **2022**, *4*, 598–604; f) C. Gao, L. Kou, H. He, *Nano-Micro Lett.* **2010**, *2*.
[18] a) P. Wang, R. K. Kankala, B. Chen, Y. Zhang, M. Zhu, X. Li, R. Long, D. Yang, R. Krastev, S. Wang, X. Xiong, Y. Liu, *ACS Appl. Mater. Interfaces* **2021**, *13*, 37563–37577; b) X. Shu, Y. Chen, P. Yan, Y. Xiang, Q. Y. Shi, T. Yin, P. Wang, L. H. Liu, X. Shuai, *J. Controlled Release* **2022**, *347*, 270–281.
[19] J. Jin, Z. Xu, Y. Zhang, Y. J. Gu, M. H. Lam, W. T. Wong, *Adv Healthc Mater* **2013**, *2*, 1501–1512.
[20] A. Natrajan, D. Sharpe, D. Wen, *Org. Biomol. Chem.* **2012**, *10*, 1883–1895.

Manuscript received: December 3, 2023
Accepted manuscript online: February 2, 2024
Version of record online: February 20, 2024